RESEARCH ARTICLE SUMMARY

CARBON CYCLE

Spaceborne detection of localized carbon dioxide sources

Florian M. Schwandner,* Michael R. Gunson, Charles E. Miller, Simon A. Carn, Annmarie Eldering, Thomas Krings, Kristal R. Verhulst, David S. Schimel, Hai M. Nguyen, David Crisp, Christopher W. O'Dell, Gregory B. Osterman, Laura T. Iraci, James R. Podolske

INTRODUCTION: Although the carbon budget is often presented in terms of global-scale fluxes, many of the contributing processes occur through localized point sources, which have been challenging to measure from space. Persistent anthropogenic carbon dioxide (CO_2) emissions have altered the natural balance of Earth's carbon sources and sinks. These emissions are driven by a multitude of individual mobile and stationary point sources that combust fossil fuels, with urban areas accounting for more than 70% of anthropogenic emissions to the atmosphere. Natural point-source emissions are dominated by wildfires and persistent volcanic degassing.

RATIONALE: Comprehensive global measurements from space could help to more completely characterize anthropogenic and natural point-source emissions. In global carbon cycle models, anthropogenic point-source information comes from bottom-up emission inventories, whereas natural point-source information comes from a sparse in situ measurement network. Whereas clusters of urban CO_2 point-source plumes merge together, isolated point sources (e.g., remote power plants, cement production plants, and persistently degassing volcanoes) create localized plumes. Because turbulent mixing and diffusion cause rapid downwind dilution, they are challenging to detect and analyze. Point-source detection from space is complicated by signal dilution: The observed values of ΔX_{CO_2} (enhancement of the column-averaged dry-air CO_2 mole fraction) correspond to in situ CO_2 enhancements of 10-fold or higher. Space-based sensors that detect and quantify CO_2 in plumes from individual point sources would enable validation of reported inventory fluxes for power plants. These sensors would also advance the detectability of volcanic eruption precursors and improve volcanic CO_2 emission inventories.

RESULTS: Spaceborne measurements of atmospheric CO_2 using kilometer-scale data from NASA's Orbiting Carbon Observatory-2 (OCO-2) reveal distinct structures caused by known anthropogenic and natural point sources, in-

cluding megacities and volcanoes. Continuous along-track sampling across Los Angeles (USA) by OCO-2 at its ~2.25-km spatial resolution exposes intra-urban spatial variability in the atmospheric X_{CO_2} distribution that corresponds to the structure of the urban dome, which is detectable under favorable wind conditions. Los Angeles X_{CO_2} peaks over the urban core and de-

creases through suburban areas to rural background values more than ~100 km away. Enhancements of X_{CO_2} in the Los Angeles urban CO_2 dome observed by OCO-2 vary seasonally from 4.4 to 6.1 parts per million (ppm). We also detected isolated CO_2 plumes from the persistently degassing Yasur, Ambrym, and Aoba volcanoes (Vanuatu), corroborated by near-simultaneous sulfur dioxide plume detections by NASA's Ozone Mapping and Profiler Suite. An OCO-2 transect passing directly downwind of Yasur volcano yielded a narrow filament of enhanced X_{CO_2} ($\Delta X_{CO_2} \approx 3.4$ ppm), consistent with plume modeling of a CO_2 point source emitting 41.6 ± 19.7 kilotons per day (15.2 ± 7.2 megatons per year). These highest continuous volcanic CO_2 emissions are collectively dwarfed by about 70 fossil fuel–burning power plants on Earth, which each emit more than 15 megatons per year of CO_2.

CONCLUSION: OCO-2's sampling strategy was designed to characterize CO_2 sources and sinks on regional to continental and ocean-basin scales, but the unprecedented kilometer-scale resolution and high sensitivity enables detection of CO_2 from natural and anthropogenic localized emission sources. OCO-2 captures seasonal, intra-urban, and isolated plume signals. Capitalizing on OCO-2's sensitivity, a much higher temporal resolution would capture anthropogenic emission signal variations from diurnal, weekly, climatic, and economic effects, and, for volcanoes, precursory emission variability. Future sampling strategies will benefit from a continuous mapping approach with the sensitivity of OCO-2 to systematically and repeatedly capture these smaller, urban to individual plume scales of CO_2 point sources. ■

XCO2 (ppm)
380 385 390 395 400 405 410
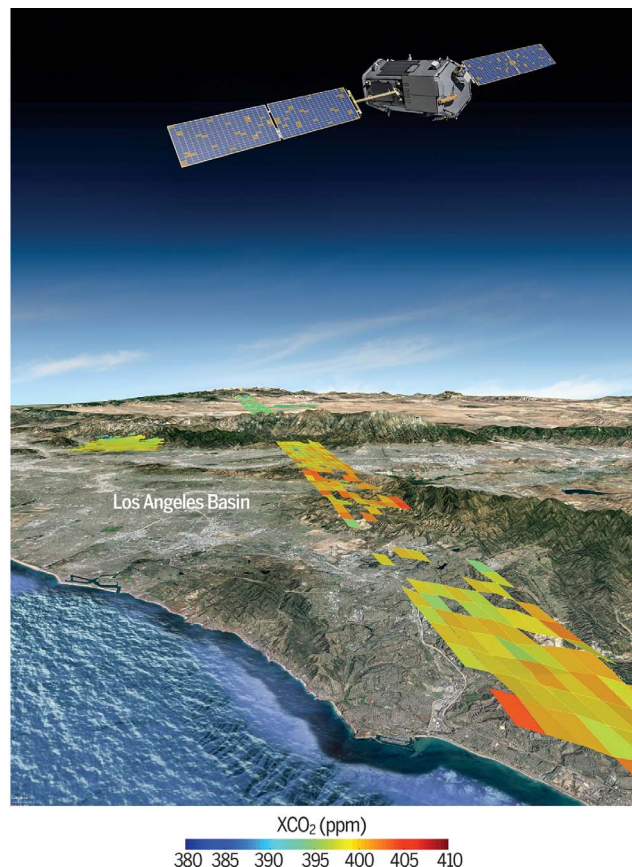
OCO-2 detects urban CO_2 signals with unprecedented detail over Los Angeles. Individual "footprints" of OCO-2 X_{CO_2} data from early fall 2014 and summer 2015 over the city of Los Angeles strongly contrast with values over the distant, rural Antelope Valley. X_{CO_2} is the averaged dry-air molar CO_2 concentration between the spacecraft and Earth's surface.

RESEARCH ARTICLE

CARBON CYCLE

Spaceborne detection of localized carbon dioxide sources

Florian M. Schwandner,[1,2]* Michael R. Gunson,[1] Charles E. Miller,[1] Simon A. Carn,[3] Annmarie Eldering,[1] Thomas Krings,[4] Kristal R. Verhulst,[1,2] David S. Schimel,[1] Hai M. Nguyen,[1] David Crisp,[1] Christopher W. O'Dell,[5] Gregory B. Osterman,[1] Laura T. Iraci,[6] James R. Podolske[6]

Spaceborne measurements by NASA's Orbiting Carbon Observatory-2 (OCO-2) at the kilometer scale reveal distinct structures of atmospheric carbon dioxide (CO_2) caused by known anthropogenic and natural point sources. OCO-2 transects across the Los Angeles megacity (USA) show that anthropogenic CO_2 enhancements peak over the urban core and decrease through suburban areas to rural background values more than ~100 kilometers away, varying seasonally from ~4.4 to 6.1 parts per million. A transect passing directly downwind of the persistent isolated natural CO_2 plume from Yasur volcano (Vanuatu) shows a narrow filament of enhanced CO_2 values (~3.4 parts per million), consistent with a CO_2 point source emitting 41.6 kilotons per day. These examples highlight the potential of the OCO-2 sensor, with its unprecedented resolution and sensitivity, to detect localized natural and anthropogenic CO_2 sources.

Although the carbon budget is often presented in terms of global-scale fluxes, many of the contributing processes actually occur through localized point sources, which have been challenging to measure from space. Persistent anthropogenic carbon dioxide (CO_2) emissions have altered the natural balance of carbon sources and sinks (*1*) and are driven by a multitude of individual mobile and stationary point sources that combust fossil fuels (*2, 3*). Urban areas account for more than 70% of anthropogenic emissions to the atmosphere (*4*). Comprehensive global measurements from space can help to more completely represent anthropogenic and natural point-source emissions in global carbon cycle models, which to date have relied on bottom-up emission inventories and a sparse in situ measurement network without independent validation on local to regional scales (*5–7*). Emissions in urban areas may occur from dense clusters of mobile and stationary point sources, leading to persistent CO_2 enhancements that produce urban CO_2 domes (*8, 9*). Isolated point sources (e.g., power plants, cement production plants, and persistently degassing volcanoes) produce individual CO_2 plumes, which have not previously been detected from space-based remote sensing platforms.

CO_2 observations from space

We present observations of CO_2 point sources from space using data from the Orbiting Carbon Observatory-2 (OCO-2) (*10*). OCO-2 is NASA's first satellite specifically designed to measure the dry-air mole fraction of CO_2 averaged over the entire atmospheric column between the ground and the satellite (X_{CO_2}) with the sensitivity, accuracy, and kilometer-scale spatial resolution needed to begin characterizing regional CO_2 sources and sinks on a global scale (*11, 12*). Launched in July 2014, OCO-2 continuously collects measurements in eight parallel <3-km^2 footprints across a narrow (<10-km) swath at 24 samples s^{-1}, either vertically along-track (nadir mode) or by following the direction of the Sun's specular reflection spot on Earth's surface (glint mode). OCO-2 leads the "afternoon constellation" of satellites (known as the A-Train) in polar orbit with a repeat cycle of 16 days (*11*). Designed to maximize the fraction of cloud-free scenes (*13*) and achieve a precision of 1 part per million (ppm) in X_{CO_2} over collections of 100 measurements, it features three grating spectrometers in the 2.06-, 1.61-, and 0.76-μm (oxygen A-band) bands to record absorption features in surface-reflected near-infrared sunlight (*11*). OCO-2 alternates between glint and nadir mode and provides up to 72,000 soundings on each of its 14.5 orbits each day. A third mode (target mode) stares at a fixed surface target, such as the ground-based validation sites of the Total Carbon Column Observing Network (TCCON) (*14, 15*), for up to 9 min as the spacecraft flies overhead, collecting up to 12,000 measurements over a ~200-km^2 area. Instrument calibration involves rigorous spectral and radiometric procedures (*11, 16–18*). More than 25 million km of OCO-2 transects have been acquired across the globe,

and these cover locations of known sources, enabling coincident observations. More than 100 million soundings have been processed (*19*), available as the operational version 7 OCO-2 X_{CO_2} data product (*19–22*). In this data set, high "warn levels," which indicate the variance of data in a selected region (*23*), can be used to identify potential localized plumes. OCO-2's contiguous soundings can be used to observe small-scale phenomena as well. Ground track locations in its three measurement modes [nadir, glint, and target mode (*24*)] do not exactly repeat each time owing to operational orbit constraints, and wind conditions change between overpasses, causing plumes to shift character and position. Consequently, OCO-2 measurements are sensitive to point sources in different locations in different orbit tracks.

The space-based vantage point offers the opportunity to detect and quantify the spatial X_{CO_2} anomalies associated with urban domes for the purpose of refining or confirming urban emission models. It also provides a means to globally assess individual volcanic point sources that may be missing from inventories (*25–27*). Here we discuss kilometer-scale spaceborne observations of two cases of localized point sources: (i) the urban CO_2 dome over the Los Angeles megacity (USA) and (ii) the isolated, persistent CO_2 plume of the passively degassing Yasur volcano (Vanuatu).

Urban CO_2 gradients

We investigated gradients between suburban, urban, and rural domains and found that seasonal patterns can be identified using OCO-2's high spatial resolution and sensitivity. The two dominant factors determining atmospheric CO_2 variability within the urban CO_2 dome are the underlying urban infrastructure (e.g., road density, industrial centers, and energy generation, distribution, and use) and atmospheric transport (*7, 8*). Uncertainties in urban carbon budgets adversely affect the performance of global carbon cycle models (*2, 4, 28–30*). Ground-based urban measurement networks have begun to address these uncertainties (*4, 31, 32*). However, some of the world's 25 largest and fastest growing megacities [e.g., Jakarta (Indonesia) and Manila (Philippines) (*33*)] lack instrumentation for systematic carbon flux measurements (*34, 35*). Simulation experiments have predicted that spaceborne measurements should detect X_{CO_2} enhancements (ΔX_{CO_2}) of 0.5 to 2 ppm over large urban centers (*36*). Recently, space-based urban greenhouse gas measurements by Japan's Greenhouse Gas Observing Satellite (GOSAT) have shown urban enhancements exceeding this prediction (ranging from 2 to 8 ppm) (*26, 37, 38*), but they provide little spatial context. However, OCO-2 measurements over large-scale industrialized regions such as North America, East Asia, and Northern Europe show that urban anthropogenic CO_2 emissions have distinct localized source signals (*39*) that require spatial context to quantify.

Continuous along-track sampling by OCO-2 at its ~2.25-km spatial resolution reveals intra-urban spatial variability in atmospheric X_{CO_2} distribution that is spatially correlated with structures of urban domes that are detectable under favorable wind

[1]Jet Propulsion Laboratory, California Institute of Technology, Pasadena, CA 91109, USA. [2]Joint Institute for Regional Earth System Science and Engineering, University of California, Los Angeles (UCLA), Los Angeles, CA 90095, USA. [3]Department of Geological and Mining Engineering and Sciences, Michigan Technological University, Houghton, MI 49931, USA. [4]Institute of Environmental Physics, University of Bremen, 28334 Bremen, Germany. [5]Department of Atmospheric Science, Colorado State University, Fort Collins, CO 80523, USA. [6]NASA Ames Research Center, Moffett Field, CA 94035, USA.
*Corresponding author. Email: fschwand@jpl.nasa.gov
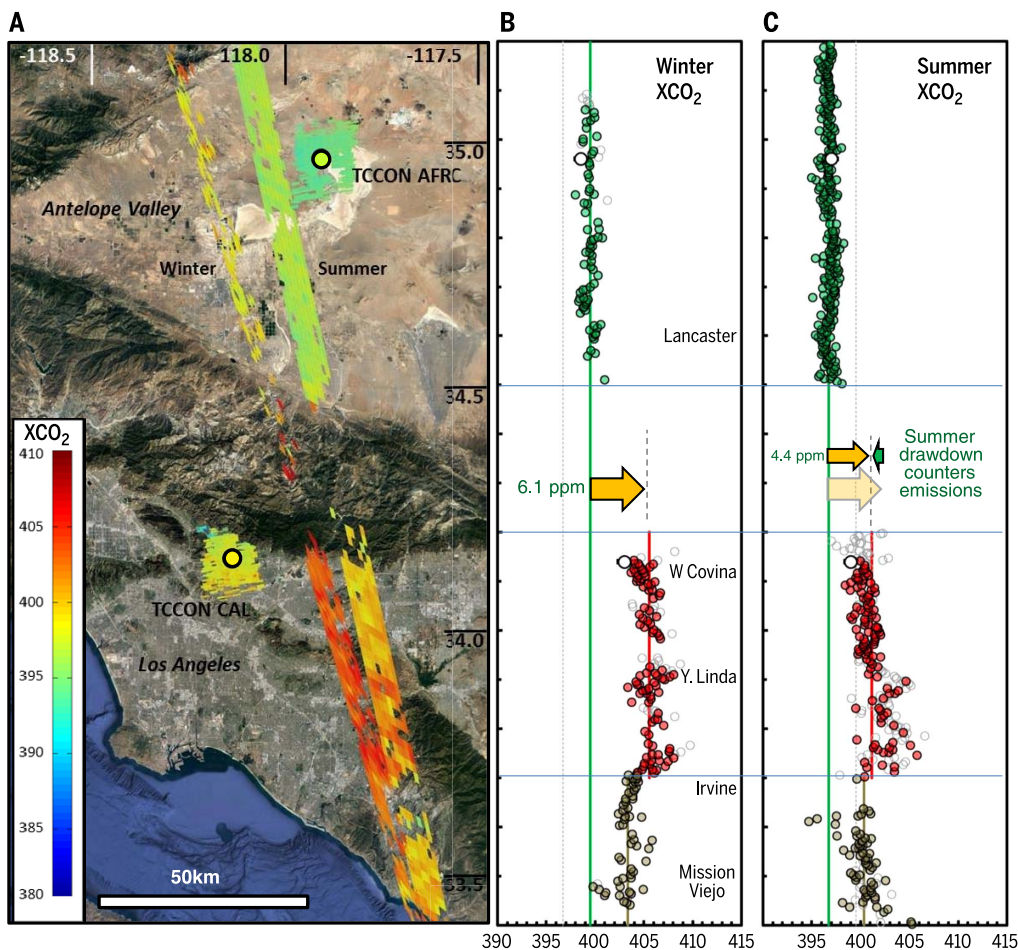
Fig. 1. OCO-2 repeatedly detects substantial urban-to-rural atmospheric CO_2 enhancements.
(**A**) Footprint visualization of OCO-2 satellite observations of atmospheric X_{CO_2} concentrations (*24*) during one representative wintertime overpass and one representative summertime overpass over the Los Angeles megacity (USA). Locations of two high-resolution ground-based spectroscopic validation stations of the Total Carbon Column Observation Network (TCCON), "CAL" and "AFRC" (*24*), are indicated. OCO-2 summer target- and nadir-mode passes show consistent seasonal differences, and ground-based TCCON values agree well with the respective OCO-2 target- and nadir-mode values. (**B** and **C**) Latitude plots in X_{CO_2} space across the same geographic domain and for the same summer and winter overpasses shown in (A). City-to-rural ΔX_{CO_2} enhancements are up to 6.1 ppm in winter, but only around 4.4 ppm in summer. Intra-urban differences along the gradient from the possibly marine layer–influenced suburbs to the higher-elevation inner city areas are distinct in both seasons. TCCON values (white circles) measured within ±30 min of the overpasses are consistent with OCO-2 data. Green circles, rural data; red circles, urban data; gray circles, urban data filtered out for quality (*24*); light brown circles, suburban data; colored lines, means (for comparison, thin gray dashed lines show the mean from the adjacent plot, and thick gray dashed lines are extensions of the red lines).

conditions. We analyzed OCO-2 data from all of its three measurement modes (nadir, glint, and target) over the greater Los Angeles megacity in the northern hemisphere summer and winter (Fig. 1) to investigate the spatial characteristics of X_{CO_2}. The greater Los Angeles area is a complex agglomerate megacity with a combined population of more than 18.5 million and a mean population density of 3198 km^{-2} [census projections (*40*)]. It is bordered by mountain ranges to the north and east and the Pacific Ocean to the south and west. Several OCO-2 nadir and glint swaths cross the area, and its dry semiarid climate permits frequent cloud-free observations. The basin is also targeted regularly for observations coinciding with those of the TCCON stations at the California Institute of Technology and the NASA Armstrong Flight Research Center. Figure 1A shows that X_{CO_2} along OCO-2 swaths increases from the rural to the suburban to urban domains of the air over Los Angeles. Irrespective of season, the urban X_{CO_2} is consistently higher than at the rural Antelope Valley desert north of Los Angeles. Within the urban domain, we detected differences between the urban core and coastal suburbs. Above these coastal suburbs, the CO_2 signal is lower than that above the urban core (Fig. 1), likely reflecting a situation where the CO_2 burden in air is in-

fluenced by a marine air layer (*41*) and where emissions from vehicle traffic and industry are less (*31*).

The plots of latitude versus X_{CO_2} in Fig. 1, B and C, further illustrate these observed differences for one representative winter and one representative summer overpass of OCO-2—capitalizing on the wealth of data that OCO-2 offers with each single overpass, which permits statistical characterization without relying on repeat observations. Zonal means, plotted as solid lines (repeated as dashed lines for comparison in the adjacent plot of the opposing season) demonstrate the contrasts between urban and rural settings and within the urban domain (urban versus suburban) (*24*). Urban-rural ΔX_{CO_2} shows seasonal differences, being largest in winter and smallest in summer. The observed winter urban-rural ΔX_{CO_2} of 6.1 ppm (13 January 2015) is consistent with previous sets of single-sounding measurements by the GOSAT instrument (*38*). In late summer 2015, the urban-rural ΔX_{CO_2} was reduced to 4.4 ppm (8 September 2015). The reduced summer ΔX_{CO_2} in this semiarid environment may reflect meteorological effects (a deeper planetary boundary layer) and possibly also a smaller contribution from previously hypothesized intra-urban photosynthetic drawdown of CO_2 (*8, 32, 42*). As a comparison with the zonal urban-rural ΔX_{CO_2}, we also calculated the ΔX_{CO_2}

between ~10- to 15-km subsets in the Pasadena suburb of Los Angeles and at the rural site; this difference was smaller than the urban-rural ΔX_{CO_2}, indicating that geophysical differences in the X_{CO_2} distribution exist within the urban domain. We confirmed this observation with simultaneously measured values obtained at close-by ground-based TCCON validation sites (Fig. 1, B and C, white circles). Furthermore, the summer urban-rural ΔX_{CO_2} measured in nadir mode is consistent with OCO-2 target mode measurements (Fig. 1). These seasonal measurements in target and nadir mode were acquired 1 year apart, showing a slight increase from 2014 to 2015, and are consistent with a globally traceable atmospheric CO_2 increase of up to 2 to 3 ppm $year^{-1}$ (*43, 44*). The seasonally repeatable magnitude of urban-rural ΔX_{CO_2} demonstrates the robustness of this urban enhancement.

Isolated CO_2 point-source plumes

We also determined whether individual isolated point-source plumes are detectable, using the example of volcanoes. In contrast to the clusters of urban CO_2 point-source plumes, which become mixed together, individual point sources form localized plumes until turbulent mixing and diffusion cause rapid downwind dilution, rendering them more challenging to detect and analyze. Even
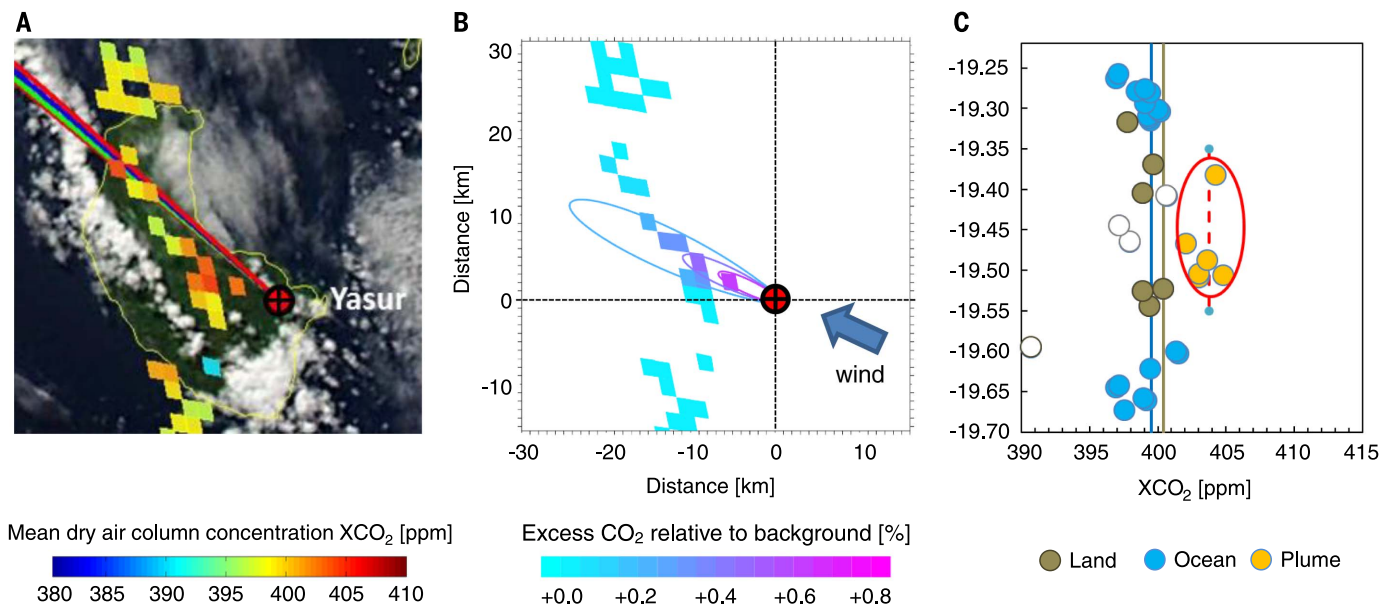
Fig. 2. OCO-2 detects a persistent CO$_2$ point-source plume from Yasur volcano on Tanna Island (Vanuatu) on 30 May 2015. Yasur volcano [red circle with black outline and cross in (A) and (B)] is persistently degassing through several active open vents and sometimes hosts a visible lava lake. It usually erupts without any interfering aerosols (mostly water vapor, CO$_2$, and SO$_2$). This measurement preceded a rare larger explosive eruption. (**A**) OCO-2 footprint visualization over concurrent MODIS true-color composite imagery, showing cloud patterns at the time of measurement and several enhanced X$_{CO_2}$ footprints. Concurrent forward wind trajectories (shown by diagonal lines extending from the vent to the northwest; different colors are multiple trajectories computed in 30-min intervals) indicate that the background air signal derives from clean, well-mixed, free remote Pacific lower tropospheric air of the Southern Hemisphere (*24*). (**B**) The order of magnitude of this detected enhancement, and the extent of the plume, correspond to a modeled CO$_2$ source strength of 41.6 ± 19.7 kilotons day^{-1} at the time of overpass (*24*), shown as model footprints and plume contours. The magnitude and extent of this plume are consistent with airborne measurements of larger fossil fuel–burning power plant point sources (*45, 46*). (**C**) The magnitude of enhancement (shown in latitude versus X$_{CO_2}$ space; compare with Fig. 1, B and C) is about 3.4 ppm near the crater vent. Blue circles, values over sea; brown circles, values over land; vertical lines, population means; white circles, aerosol- or cloud-affected soundings (*24*). The red oval highlights the volcanic plume data (gold circles); the red dashed line is the plume mean, with blue end nodes denoting the extent of the detectable plume.

some of the largest individual emission sources can become indistinguishable from the background within just 10 to 15 km of the source (*45, 46*). Power plants and persistently active volcanoes continuously emit CO$_2$ into the atmosphere, resulting in isolated short-range CO$_2$ plumes. Natural volcanic CO$_2$ point sources, dominated by non-eruptive episodic and persistent degassing activity, are an integral part of the planetary carbon cycle (*47–49*). Volcanic "passive" persistent degassing occurs via crater plumes and fault systems and through widespread diffuse flank degassing, and degassing from crater lakes (*49, 50*). Volcanic emissions of CO$_2$ to date have not been detected from space—from either persistently degassing or explosively erupting volcanoes. The ~450 active subaerial volcanoes on Earth emit CO$_2$ persistently at an estimated global source strength of 0.54 gigatons year^{-1} (*49*), a minor source compared with anthropogenic CO$_2$ emissions, now estimated at 35.9 to 38.2 gigatons year^{-1} (*2, 3*). Volcanic CO$_2$ emissions correlate with rates of magma production and proximity of magma to the surface (which are also expressed as heat emissions) (*49*). Considerable temporary increases in CO$_2$ emissions, the main dry-gas component, often precede eruptions (*51*) but may go unnoticed, particularly in remote areas where no in situ instrumentation is deployed. The National Academies identified the ability

to measure passive volcanic CO$_2$ degassing from space as one of the grand challenges and key research and observation priorities in volcano science (*52*).

We detected one isolated volcanic plume with OCO-2 at Yasur volcano on 30 May 2015 (Fig. 2). The background concentration field is very flat and homogenous owing to the lack of strong local sources (other than Vanuatu's volcanoes) in this remote region of the southwestern Pacific. OCO-2 data from this glint-mode overpass show several footprints with substantially elevated X$_{CO_2}$ within 15 km downwind of the known continuous gas emission point of Yasur volcano. The wind and plume direction are corroborated by a nearby cloud trail shown in an image acquired by the MODIS (Moderate Resolution Imaging Spectroradiometer) instrument aboard NASA's Aqua satellite within a few minutes of the OCO-2 measurement (underlain in Fig. 2). We analyzed the plume's direction from this OCO-2 overpass over Yasur volcano by forward-trajectory modeling using the Hybrid Single Particle Lagrangian Integrated Trajectory Model [HYSPLIT, wind fields from the Global Data Assimilation System 1 at 0.5° resolution (*53*)] in half-hourly intervals beginning at 400 m above sea level, which is ~40 m above the highest topographic point near the volcano's summit. The results in Fig. 2A (colored lines) are consistent

with local airport measurements during the time of the overpass, with a wind speed of 4 m s^{-1} and a southeasterly direction [Burton field, Tanna Island, Meteorological Terminal Aviation Routine (METAR) data (*54*)]. This analysis confirms that the observed CO$_2$ enhancement originates from Yasur volcano.

Being able to quantify the CO$_2$ emissions of isolated plumes from individual point sources would advance the detectability of volcanic eruption precursors and volcanic CO$_2$ emission inventories, and it would likewise enable validation of reported inventory fluxes for power plants. We modeled this plume's CO$_2$ flux at the overpass time and inverted the plume X$_{CO_2}$ data using a Gaussian plume model at known wind speed (*24*). Results in Fig. 2B trace the same plume direction as the observational data set and simulate the enhancement of the same footprints, confirming the pattern observed in the OCO-2 data set. The resulting enhancement of the Gaussian plume, contoured, is best explained by a CO$_2$ source strength of 41.6 ± 19.7 kilotons day^{-1} (15.18 ± 7.19 megatons year^{-1}), which is consistent with plume measurements and plume models for power plants with similar CO$_2$ emission strength and plume extent (*45, 46*). The error on the inversion result is derived from the standard deviation of excess CO$_2$ in a radius of about 170 km around the island, giving about

Fig. 3. OCO-2 detects CO$_2$ enhancements in two persistent non-eruptive point-source plumes over Aoba and Ambrym volcanoes (Vanuatu) on 22 November 2015. (**A**) OCO-2 footprint visualization at Aoba volcano over concurrent MODIS true-color composite imagery, showing a considerable localized enhancement (mean ΔX_{CO_2} = 5.5 ppm) directly above and downwind of its strongly degassing acid crater lake. (**B**) OCO-2 footprint visualization at Ambrym volcano over concurrent MODIS true-color composite imagery, showing a very localized peripheral enhancement (mean ΔX_{CO_2} = 2.8 ppm) flanking the westward-drifting plume, diminishing with distance from the vent. The color scale in (A) and (B) is as in Fig. 2. (**C**) OCO-2 flew over Vanuatu at 02:23–02:24 UTC (orbit 07395) in glint mode [details in (A) and (B)], and the OMPS instrument aboard the Suomi-NPP satellite flew over just 4 min later (02:27–02:29 UTC,

orbit 21079). These observations corroborate the volcanic ΔX_{CO_2} through X_{SO_2} plume detections from the westward-drifting volcanic plumes. A fainter SO$_2$ plume is visible extending west from Yasur. OMPS has lower spatial resolution than OCO-2 (~50 by 50 km), evinced by its ~10-km-wide swath outline. PCA, principal component analysis–based retrieval algorithm (*69*); PBL, planetary boundary layer; DU, Dobson units.
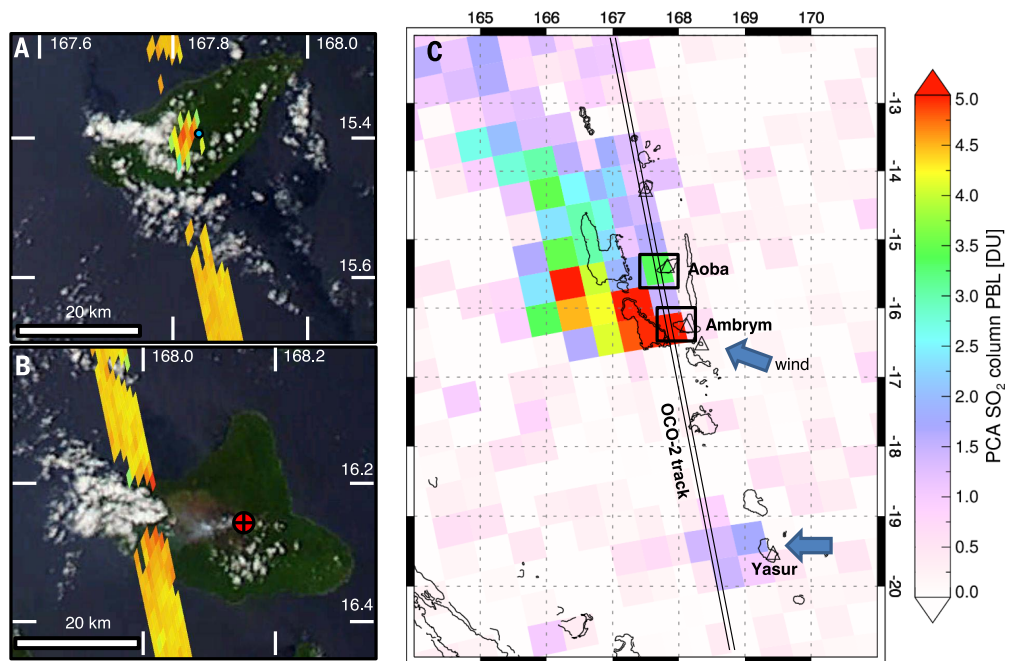
0.4% (1σ). This is an estimate for the relative accuracy of the measurements entering the inversion algorithm and subsequently yielding a relative error of about 47% on the emission rate.

This estimate is an order of magnitude higher than expected CO$_2$ fluxes at Yasur (*55*, *56*), and some uncorrected bias may still skew the data (*24*). However, circumstantial information is consistent with higher emissions during this first spaceborne volcanic CO$_2$ detection. The volcano was thermally very active in May and June 2015, and particularly from 27 to 31 May: Its peak upwelling thermal infrared signal for the year was detected by MODIS on 31 May 2015, the day after the OCO-2 overpass (*24*). The MODIS thermal observations indicate elevated heat flux directly succeeding the OCO-2 measurement, likely reflecting high levels of Strombolian activity at Yasur. Indeed, the Vanuatu Geohazards Observatory reports Strombolian eruptions from 29 to 31 May 2015, and this type of activity can be driven by very strong CO$_2$ degassing (*57*). Because eruptive events are gas-driven and CO$_2$ is known to herald eruptions (*51*, *58*–*61*), it is conceivable that the volcano's CO$_2$ emissions were particularly elevated around the time of the OCO-2 overpass, exceeding the high persistent CO$_2$ emissions expected from this source. During and before such Strombolian activity phases, the ratio of CO$_2$ to sulfur dioxide (SO$_2$) emissions can increase by an order of magnitude (*57*). Yasur is among the strongest known continuous volcanic gas emitters on Earth, based on SO$_2$ measurements (*62*), and with CO$_2$ usually being the more dominant gas species, we would expect it to be substantially enhanced relative to the background even if it was not followed by, or coincident with, a strong

thermal and/or Strombolian event. This very strong enhancement is likely temporary, and the coincident measurement by OCO-2 was fortuitous. Although the confounding effects of sulfate aerosol and water vapor in the plume (*63*), topography, and albedo are not yet individually constrained in the data or the inversion, the reasonable inverse flux result within the same order of magnitude as expected fluxes is compelling.

The observation of a strong CO$_2$ plume associated with Yasur's Strombolian activity is corroborated by additional detections of volcanic CO$_2$ and SO$_2$ plume signals from nearby volcanoes (Fig. 3). This is no surprise given that the Vanuatu volcanic arc contains some of the world's strongest sources of volcanic gas emissions. A recent satellite-based inventory of volcanic SO$_2$ emissions (*64*) ranked Ambrym, Aoba (also known as Ambae), and Yasur first, fifth, and 11th (respectively) in terms of mean SO$_2$ flux in a list of 91 detectable, persistent volcanic SO$_2$ sources, on the basis of satellite measurements from 2005 to 2015. Furthermore, Ambrym, Aoba, and Yasur all show increasing trends in SO$_2$ flux over the decade of observation, with above-average emissions in 2015 (*62*, *64*, *65*). Satellite observations on the day of the OCO-2 measurements (Fig. 3) appeared typical and consistent with the relative source strengths of the three volcanoes. Ambrym hosts at least two active basaltic lava lakes (*66*, *67*), Aoba has an acid crater lake at its summit (*68*), and Yasur exhibits persistent open-vent degassing and episodic Strombolian explosive activity (*55*). On 22 November 2015, OCO-2 passed too far from Yasur for there to be a meaningful imprint of the volcano's CO$_2$ plume on the acquired data. However, the 22 November 2015 overpass

by the OMPS (Ozone Mapping and Profiler Suite) aboard the Suomi-NPP (Suomi–National Polar-orbiting Partnership) satellite, shown in Fig. 3C, occurred only ~4 to 5 min after the OCO-2 overpass shown in Fig. 3, A and B, and confirms the degassing plume positions, consistent with METAR wind information (*54*). Using the algorithm described by (*69*), SO$_2$ mass retrievals in the OMPS data frame shown here yield about 6.23 kilotons of SO$_2$ (*24*). At the time of these detections, Ambrym was at alert level 2 and Aoba at alert level 1, according to reports by the Vanuatu Geohazards Observatory. These multiple detections, corroborated by near-simultaneous SO$_2$ plume retrievals, unambiguously demonstrate the capability of OCO-2 to detect strong localized CO$_2$ plumes. Such plumes extend at most 10 to 20 km from the source before becoming undetectable by OCO-2.

Conclusions

We demonstrated that localized urban CO$_2$ sources and volcanic CO$_2$ plumes are detectable from space using OCO-2. We found that anthropogenic CO$_2$ emissions from within the Los Angeles megacity result in persistent enhancements of 4 to 6 ppm within the urban dome, consistent with previous observations (*25*). Additionally, OCO-2 enabled us to quantify the seasonally dependent urban-suburban-rural gradient, which compares well with ground-based measurements from the Los Angeles Megacity network (*31*, *37*, *41*). The ~2-km^2 spatial resolution, contiguous down-track sampling, and high detection sensitivity of OCO-2 have also enabled us to detect intense individual CO$_2$ plumes with their expected few kilometers of extent and small enhancement. Comparison of measured

and modeled source strengths for Yasur volcano (Vanuatu) confirm that we have detected and quantified volcanic CO_2 emissions from space. Our results demonstrate that the emissions from one of the largest continuous volcanic CO_2 emitters on Earth (*49*, *62*, *64*, *65*), similar in source strength to a large coal-fired power plant, barely reach the lower end of the range of emissions from the ~70 largest fossil fuel–burning power plants on Earth [(*70*), last accessed 30 April 2017], which themselves are dwarfed by megacity emissions (*4*).

These successes testify to the capability of space-borne sampling of patterns of natural and fossil fuel emissions, as expressed in their atmospheric signatures or gradients. The types of CO_2 sources investigated here represent the majority of anthropogenic and abiotic-natural CO_2 point sources contributing to the carbon cycle.

The OCO-2 sampling strategy was designed to infer CO_2 sources and sinks on regional to continental and ocean-basin scales (*10*). OCO-2 by far exceeds design specifications by being able to detect localized point-source plume signals and megacity emissions in single overpasses, as demonstrated here. The localized sources detected to date have been serendipitous intersections of the OCO-2 observation path with source plumes or urban domes. OCO-2 samples only ~7% of the Earth's surface, and the observing strategy was not optimized for point-source detection. Nonetheless, OCO-2's high measurement sensitivity and spatial resolution (small footprints) demonstrate the capability to detect and quantify point sources and will prove useful for spot-checking estimates of megacity emissions, volcanic activity, and other localized sources of similar magnitude. OCO-2 provides some spatial context at the kilometer scales appropriate to localized sources. The SCIAMACHY (SCanning Imaging Absorption spectroMeter for Atmospheric CHartographY) instrument aboard the European Envisat platform provided X_{CO_2} measurements at a spatial resolution of 30 by 60 km (until it ceased to communicate in 2012)—too coarse to detect most localized point-source plumes (*71*). GOSAT can frequently target point sources at a 3-day repeat cycle (*38*), but its measurements lack spatial context owing to its coarser sampling pattern and its large footprint (>10 km in diameter).

OCO-2 data and observation methods have demonstrated the capabilities of X_{CO_2} observations in kilometer-scale spatial resolution, pointing ahead to future greenhouse gas mapping applications from space. Seasonal signals are clearly trackable in the OCO-2 data, but the known diurnal, weekly, climatic, and economic effects on anthropogenic emission signals (*31*, *41*) require shorter return intervals than currently performed by OCO-2. Future sampling strategies will benefit from a continuous mapping approach to systematically and repeatedly capture these smaller, urban to individual plume scales of CO_2 point sources. Persistent contiguous observations with OCO-2–like sensitivity from a geostationary orbit would be required to overcome limitations from a single low-Earth-orbiting system to continuously observe anthropogenic and natural emissions and to enable point-source attribution (*4*, *72*).

The fortuitous detection and quantification of CO_2 sources by OCO-2 demonstrated here open a path toward contiguous regional mapping capabilities with OCO-2–like sensitivity in future missions such as NASA's OCO-3 (scheduled to launch in 2018) (*73*) and GeoCARB (Geostationary Carbon Cycle Observatory) (*74*, *75*).

Materials and methods
Bias correction

A correction is applied to correct significant biases that are found to correlate to surface pressure, aerosol optical depth, and other factors (*19*). For small-scale individual plume analysis, it may be argued not to use the mostly globally applied standard product bias correction. The bias correction was determined from large-scale homogenous data fields, not from small scale variability typical of localized point-source plumes. Individual feature corrections (*19*) may incorrectly represent discrepancies on a footprint-to-footprint scale, especially for strong localized sources. However, this is negligible on this observed scale given the sufficient number of soundings per observed population of values (Fig. 1, B and C). Specifically applied for the Los Angeles data set, bias correction corrects for some global and individual artifacts, leading to more Gaussian populations of the investigated domains, and to a shift of X_{CO_2} domain population means by 1.7 to 2 ppm. CO_2 signals may in some cases be strongly influenced by aerosol signals and rough terrain. Some work remains to optimize data retrievals for the impact of aerosols, cloud shadows, and rough terrain, and hence, to improve bias correction. However, independent verification of the Los Angeles megacity CO_2 enhancements by TCCON ground-based reference data validate our findings, and in both case studies, aerosol optical depth and terrain influences have been found to be minimal. The remaining global biases do not significantly impact the results within the small spatial domains analyzed here.

Inverse modeling

The observed enhancements (Fig. 2B) are consistent with an inverse Gaussian plume model showing 10.4 ± 4.9 kilotons day^{-1} CO_2 per unit wind speed (meters per second), at 4 m s^{-1} wind speed at that time [Burton field, Tanna Island, METAR data (*54*)], using a land X_{CO_2} mean from Tanna Island and neighboring islands from the same orbit. The inversion was performed very similar to reported methods (*46*) by inverting a Gaussian plume model and accounting for atmospheric stability (which affects plume width). Here, the target value was emission rate per unit wind speed. A loose constraint on the stability parameter (156 ± 100) and basically no constraints on the emission rate were applied. The local background was determined from the median of all available X_{CO_2} data over land (400.4 ppm). This prevents any effects from the known land/sea bias but leads potentially to a slightly overestimated background and subsequently an underestimated emission rate. This is due to the fact that some of the footprints may be impacted by the volcanic CO_2 emissions. Absolute excess amounts of CO_2 with respect to the local background, which are input for the inversion, were computed accounting for surface pressure.

The median over the larger area (radius of about 170 km, including the islands) gives a background of about 399.5 ppm X_{CO_2}. Excluding the island, the background is slightly lower, but still rounds to 399.5 ppm. This also reflects the robustness of the median. Reasons for the difference between land and ocean background are the known land/sea bias in OCO-2 glint observations (*11*, *19*).

TCCON data screening

The data sets visualized in Fig. 1A were composed using Google Earth over Landsat composite imagery (USGS) and include: winter glint mode pass on 13 January 2015 (orbit no. 02848), summer nadir mode pass on 8 September 2015 (orbit no. 06314), as well as two OCO-2 target mode data sets acquired over Pasadena in northern Los Angeles (orbit no. 01392 on 5 October 2014), and over NASA's Armstrong Flight Research Center (AFRC) in rural Antelope Valley (orbit no. 01421 on 7 October 2014). At the northern suburb of Pasadena, one of the 23 global TCCON ground validation sites is hosted by the California Institute of Technology (site named CAL in Fig. 1A), and another TCCON site is situated in the rural Antelope Valley region, at the AFRC, both of which are frequently measured by OCO-2 in target mode. OCO-2 target mode data over these TCCON sites were screened using screen parameters numbered 1, 2, 5, and 9 reported elsewhere (*15*). Grayed-out data points in Fig. 1, B and C, were excluded based on quality filtering (retrieved *surface roughness* parameter, cutoff at value = 40), though inclusion does not alter the results in a significant way, which testifies to the robustness of these measurements.

Excess X_{CO_2} over Tanna Island (Vanuatu)

Figure 2A shows data visualized from OCO-2's glint orbit no. 04832 (path number 194, standard level 2 retrieval product data, version 7). Figure 2A superimposes OCO-2 data over visible (true-color composite) imagery acquired by the MODIS instrument aboard the Aqua satellite. Figure 2C vertical lines are population means: land mean X_{CO_2} (brown line) derived from high quality soundings over Tanna and adjacent Erromango island, Vanuatu, soundings with the oxygen A-band's retrieval goodness-of-fit $\chi^2 > 5$ grayed out for likely being cloud-contaminated. Ocean mean X_{CO_2} (blue line) plotted as reference, showing the expected low land-sea bias in the glint data (*11*, *19*). Blue-scale footprints in Fig. 2B are a synthetic reconstruction from the inverse model showing percent enhancement above background, and plume contours denote 0.2, 0.4, and 0.6% modeled enhancements.

REFERENCES AND NOTES

1. P. Friedlingstein *et al*., Persistent growth of CO_2 emissions and implications for reaching climate targets. *Nat. Geosci.* **7**, 709–715 (2014). doi: 10.1038/ngeo2248
2. C. Le Quéré *et al*., Global Carbon Budget 2015. *Earth Syst. Sci. Data* **7**, 349–396 (2015). doi: 10.5194/essd-7-349-2015
3. G. Peters *et al*., The challenge to keep global warming below 2° C. *Nat. Clim. Chang.* **3**, 4–6 (2013). doi: 10.1038/nclimate1783

4. R. Duren, C. Miller, Measuring the carbon emissions of megacities. *Nat. Clim. Chang.* **2**, 560–562 (2012). doi: 10.1038/nclimate1629

5. T. Oda, S. Maksyutov, A very high-resolution (1 km×1 km) global fossil fuel CO_2 emission inventory derived using a point source database and satellite observations of nighttime lights. *Atmos. Chem. Phys.* **11**, 543–556 (2011). doi: 10.5194/acp-11-543-2011

6. M. G. Hutchins, J. D. Colby, G. Marland, E. Marland, A comparison of five high-resolution spatially-explicit, fossil-fuel, carbon dioxide emission inventories for the United States. *Mitig. Adapt. Strategies Glob. Change* **22**, 947–972 (2016).

7. T. Lauvaux et al., High-resolution atmospheric inversion of urban CO_2 emissions during the dormant season of the Indianapolis Flux Experiment (INFLUX). *J. Geophys. Res. D Atmospheres* **121**, 5213–5236 (2016). doi: 10.1002/2015JD024473

8. S. Feng et al., Los Angeles megacity: A high-resolution land–atmosphere modelling system for urban CO_2 emissions. *Atmos. Chem. Phys.* **16**, 9019–9045 (2016). doi: 10.5194/acp-16-9019-2016

9. C. Idso, S. Idso, R. Balling Jr., The urban CO_2 dome of Phoenix, Arizona. *Phys. Geogr.* **19**, 95–108 (1998).

10. A. Eldering, The Orbiting Carbon Observatory-2 early science investigations of regional carbon dioxide fluxes. *Science* **358**, eaam5745 (2017).

11. D. Crisp et al., The on-orbit performance of the Orbiting Carbon Observatory-2 (OCO-2) instrument and its radiometrically calibrated products. *Atmos. Meas. Tech.* **10**, 59–81 (2016). doi: 10.5194/amt-10-59-2017

12. C. Miller et al., Precision requirements for space-based X_{CO2} data. *J. Geophys. Res. D Atmospheres* **112**, D10314 (2007). doi: 10.1029/2006JD007659

13. T. Taylor et al., Orbiting Carbon Observatory-2 (OCO-2) cloud screening algorithms: Validation against collocated MODIS and CALIOP data. *Atmos. Meas. Tech.* **9**, 973–989 (2016). doi: 10.5194/amt-9-973-2016

14. D. Wunch et al., The total carbon column observing network. *Philos. Trans. A Math. Phys. Eng. Sci.* **369**, 2087–2112 (2011). doi: 10.1098/rsta.2010.0240

15. D. Wunch et al., Comparisons of the Orbiting Carbon Observatory-2 (OCO-2) X_{CO2} measurements with TCCON. *Atmos. Meas. Tech.* **10**, 2209–2238 (2017). doi: 10.5194/amt-10-2209-2017

16. C. O'Dell et al., Preflight radiometric calibration of the orbiting carbon observatory. *IEEE Trans. Geosci. Remote Sens.* **49**, 2438–2447 (2011). doi: 10.1109/TGRS.2010.2090887

17. J. Day et al., Preflight spectral calibration of the Orbiting Carbon Observatory. *IEEE Trans. Geosci. Remote Sens.* **49**, 2793–2801 (2011). doi: 10.1109/TGRS.2011.2107745

18. C. Frankenberg et al., The Orbiting Carbon Observatory (OCO-2): Spectrometer performance evaluation using pre-launch direct sun measurements. *Atmos. Meas. Tech.* **8**, 301–313 (2014). doi: 10.5194/amt-8-301-2015

19. A. Eldering et al., The Orbiting Carbon Observatory-2: First 18 months of science data products. *Atmos. Meas. Tech.* **10**, 549–563 (2017). doi: 10.5194/amt-10-549-2017

20. D. Crisp et al., The ACOS CO_2 retrieval algorithm-Part II: Global X_{CO2} data characterization. *Atmos. Meas. Tech.* **5**, 687–707 (2012). doi: 10.5194/amt-5-687-2012

21. C. O'Dell et al., The ACOS CO_2 retrieval algorithm-Part 1: Description and validation against synthetic observations. *Atmos. Meas. Tech.* **5**, 99–121 (2012). doi: 10.5194/amt-5-99-2012

22. G. Osterman et al., "Orbiting Carbon Observatory-2 (OCO-2) data product user's guide, operational L1 and L2 data versions 7 and 7R" (NASA Jet Propulsion Laboratory, California Institute of Technology, 2015); https://co2.jpl.nasa.gov/static/docs/OCO2_DUG_150911_VerF2.pdf.

23. L. Mandrake et al., Semi-autonomous sounding selection for OCO-2. *Atmos. Meas. Tech.* **6**, 2851–2864 (2013). doi: 10.5194/amt-6-2851-2013

24. Materials and methods.

25. E. Kort, W. Angevine, R. Duren, C. Miller, Surface observations for monitoring urban fossil fuel CO_2 emissions: Minimum site location requirements for the Los Angeles megacity. *J. Geophys. Res. D Atmospheres* **118**, 1577–1584 (2013). doi: 10.1002/jgrd.50135

26. R. Janardanan et al., Comparing GOSAT observations of localized CO_2 enhancements by large emitters with inventory-based estimates. *Geophys. Res. Lett.* **43**, 3486–3493 (2016). doi: 10.1002/2016GL067843

27. F. M. Schwandner, "The Orbiting Carbon Observatory 2 – Opportunities for deep carbon research" (Deep Carbon Observatory, 2014); https://deepcarbon.net/feature/orbiting-carbon-observatory-2---opportunities-deep-carbon-research.

28. D. Dodman, Blaming cities for climate change? An analysis of urban greenhouse gas emissions inventories. *Environ. Urban.* **21**, 185–201 (2009). doi: 10.1177/0956247809103016

29. K. R. Gurney, Recent research quantifying anthropogenic CO_2 emissions at the street scale within the urban domain. *Carbon Manag.* **5**, 309–320 (2014). doi: 10.1080/17583004.2014.986849

30. C. Le Quéré et al., Trends in the sources and sinks of carbon dioxide. *Nat. Geosci.* **2**, 831–836 (2009). doi: 10.1038/ngeo689

31. K. Verhulst et al., Carbon dioxide and methane measurements from the Los Angeles Megacity Carbon Project: 1. Calibration, urban enhancements, and uncertainty estimates. *Atmos. Chem. Phys.* **17**, 8313–8314 (2017). doi: 10.5194/acp-17-8313-2017

32. J. Turnbull et al., Toward quantification and source sector identification of fossil fuel CO_2 emissions from an urban area: Results from the INFLUX experiment. *J. Geophys. Res. D Atmospheres* **120**, 292–312 (2015). doi: 10.1002/2014JD022555

33. UN Department of Economic and Social Affairs, Population Division, "World urbanization prospects: The 2014 revision" (UN, 2014); https://esa.un.org/unpd/wup/CD-ROM/.

34. R. Macatangay et al., Factors influencing surface CO_2 variations in LPRU, Thailand and IESM, Philippines. *Environ. Pollut.* **195**, 282–291 (2014). doi: 10.1016/j.envpol.2014.06.035; pmid: 25056588

35. P. K. Patra, J. G. Canadell, S. Lal, The rapidly changing greenhouse gas budget of Asia. *EOS Trans.* **93**, 237 (2012). doi: 10.1029/2012EO250006

36. S. Pacala, R. Socolow, Stabilization wedges: Solving the climate problem for the next 50 years with current technologies. *Science* **305**, 968–972 (2004). doi: 10.1126/science.1100103; pmid: 15310891

37. D. Wunch, P. O. Wennberg, G. C. Toon, G. Keppel-Aleks, Y. G. Yavin, Emissions of greenhouse gases from a North American megacity. *Geophys. Res. Lett.* **36**, L15810 (2009). doi: 10.1029/2009GL039825

38. E. Kort, C. Frankenberg, C. Miller, T. Oda, Space-based observations of megacity carbon dioxide. *Geophys. Res. Lett.* **39**, L17806 (2012). doi: 10.1029/2012GL052738

39. J. Hakkarainen, I. Ialongo, J. Tamminen, Direct space-based observations of anthropogenic CO_2 emission areas from OCO-2. *Geophys. Res. Lett.* **43**, 11400–11406 (2016). doi: 10.1002/2016GL070885

40. U. S. Census Bureau, "United States Census 2010" (U.S. Census Bureau, 2010); www.census.gov/2010census/.

41. S. Newman et al., Diurnal tracking of anthropogenic CO_2 emissions in the Los Angeles basin megacity during spring 2010. *Atmos. Chem. Phys.* **13**, 4359–4372 (2013). doi: 10.5194/acp-13-4359-2013

42. W. Wang, D. Pataki, Spatial patterns of plant isotope tracers in the Los Angeles urban region. *Landsc. Ecol.* **25**, 35–52 (2010). doi: 10.1007/s10980-009-9401-5

43. A. P. Ballantyne, C. B. Alden, J. B. Miller, P. P. Tans, J. W. White, Increase in observed net carbon dioxide uptake by land and oceans during the past 50 years. *Nature* **488**, 70–72 (2012). doi: 10.1038/nature11299; pmid: 22859203

44. E. Dlugokencky, P. Tans, "Trends in atmospheric carbon dioxide" (Earth System Research Laboratory, National Oceanic and Atmospheric Administration, 2016).

45. H. Bovensmann et al., A remote sensing technique for global monitoring of power plant CO_2 emissions from space and related applications. *Atmos. Meas. Tech.* **3**, 781–811 (2010). doi: 10.5194/amt-3-781-2010

46. T. Krings et al., MAMAP–A new spectrometer system for column-averaged methane and carbon dioxide observations from aircraft: Retrieval algorithm and first inversions for point source emission rates. *Atmos. Meas. Tech.* **4**, 1735–1758 (2011). doi: 10.5194/amt-4-1735-2011

47. J. Gaillardet, A. Galy, Himalaya—carbon sink or source? *Science* **320**, 1727–1728 (2008). doi: 10.1126/science.1159279; pmid: 18583600

48. P. B. Kelemen, C. E. Manning, Reevaluating carbon fluxes in subduction zones, what goes down, mostly comes up. *Proc. Natl. Acad. Sci. U.S.A.* **112**, E3997–E4006 (2015). doi: 10.1073/pnas.1507889112; pmid: 26048906

49. M. Burton, G. Sawyer, D. Granieri, Deep carbon emissions from volcanoes. *Rev. Mineral. Geochem.* **75**, 323–354 (2013). doi: 10.2138/rmg.2013.75.11

50. A. Mazot et al., CO_2 discharge from the bottom of volcanic Lake Rotomahana, New Zealand. *Geochem. Geophys. Geosyst.* **15**, 577–588 (2014). doi: 10.1002/2013GC004945

51. J. M. de Moor et al., Turmoil at Turrialba Volcano (Costa Rica): Degassing and eruptive processes inferred from high-frequency gas monitoring. *J. Geophys. Res. Solid Earth* **121**, 5761–5775 (2016). doi: 10.1002/2016JB013150; pmid: 27774371

52. National Academies of Sciences, *Volcanic Eruptions and Their Repose, Unrest, Precursors, and Timing* (National Academies Press, 2017).

53. A. Stein et al., NOAA's HYSPLIT atmospheric transport and dispersion modeling system. *Bull. Am. Meteorol. Soc.* **96**, 2059–2077 (2015). doi: 10.1175/BAMS-D-14-00110.1

54. Unidata/University Corporation for Atmospheric Research, "Historical Unidata Internet Data Distribution (IDD) global observational data, May 2003 - current" (National Center for Atmospheric Research, 2003); http://rda.ucar.edu/datasets/ds336.0/).

55. C. Oppenheimer, P. Bani, J. Calkins, M. Burton, G. Sawyer, Rapid FTIR sensing of volcanic gases released by Strombolian explosions at Yasur volcano, Vanuatu. *Appl. Phys. B* **85**, 453–460 (2006). doi: 10.1007/s00340-006-2353-4

56. N. Métrich et al., Magma and volatile supply to post-collapse volcanism and block resurgence in Siwi Caldera (Tanna Island, Vanuatu Arc). *J. Petrol.* **52**, 1077–1105 (2011). doi: 10.1093/petrology/egr019

57. A. Aiuppa et al., First observational evidence for the CO_2-driven origin of Stromboli's major explosions. *Solid Earth* **2**, 135–142 (2011). doi: 10.5194/se-2-135-2011

58. C. Werner et al., Deep magmatic degassing versus scrubbing: Elevated CO_2 emissions and C/S in the lead-up to the 2009 eruption of Redoubt Volcano, Alaska. *Geochem. Geophys. Geosyst.* **13**, Q03015 (2012). doi: 10.1029/2011GC003794

59. A. Aiuppa et al., Unusually large magmatic CO_2 gas emissions prior to a basaltic paroxysm. *Geophys. Res. Lett.* **37**, L17303 (2010). doi: 10.1029/2010GL043837

60. M. Liuzzo, S. Gurrieri, G. Giudice, G. Giuffrida, Ten years of soil CO_2 continuous monitoring on Mt. Etna: Exploring the relationship between processes of soil degassing and volcanic activity. *Geochem. Geophys. Geosyst.* **14**, 2886–2899 (2013). doi: 10.1002/ggge.20196

61. J. Rosen, Gas changes signal eruptions. *Science* **354**, 952–953 (2016). doi: 10.1126/science.354.6315.952; pmid: 27884984

62. S. Carn, L. Clarisse, A. Prata, Multi-decadal satellite measurements of global volcanic degassing. *J. Volcanol. Geotherm. Res.* **311**, 99–134 (2016). doi: 10.1016/j.jvolgeores.2016.01.002

63. A. Butz, O. P. Hasekamp, C. Frankenberg, I. Aben, Retrievals of atmospheric CO_2 from simulated space-borne measurements of backscattered near-infrared sunlight: Accounting for aerosol effects. *Appl. Opt.* **48**, 3322–3336 (2009). doi: 10.1364/AO.48.003322; pmid: 19543338

64. S. A. Carn, V. E. Fioletov, C. A. McLinden, C. Li, N. A. Krotkov, A decade of global volcanic SO_2 emissions measured from space. *Sci. Rep.* **7**, 44095 (2017). doi: 10.1038/srep44095; pmid: 28275238

65. P. Bani et al., First volcanic SO_2 budget for the Vanuatu archipelago. *J. Volcanol. Geotherm. Res.* **211**, 36–46 (2012). doi: 10.1016/j.jvolgeores.2011.10.005

66. P. Bani et al., Surge in sulfur and halogen degassing from Ambrym volcano, Vanuatu. *Bull. Volcanol.* **71**, 1159–1168 (2009). doi: 10.1007/s00445-009-0293-7

67. P. Allard et al., Prodigious emission rates and magma degassing budget of major, trace and radioactive volatile species from Ambrym basaltic volcano, Vanuatu island Arc. *J. Volcanol. Geotherm. Res.* **322**, 119–143 (2016). doi: 10.1016/j.jvolgeores.2015.10.004

68. P. Bani et al., Remarkable geochemical changes and degassing at Voui crater lake, Ambae volcano, Vanuatu. *J. Volcanol. Geotherm. Res.* **188**, 347–357 (2009). doi: 10.1016/j.jvolgeores.2009.09.018

69. C. Li et al., New-generation NASA Aura Ozone Monitoring Instrument volcanic SO_2 dataset: Algorithm description, initial results, and continuation with the Suomi-NPP Ozone Mapping and Profiler Suite. *Atmos. Meas. Tech.* **10**, 445–458 (2017). doi: 10.5194/amt-10-445-2017

70. CARMA, Carbon Monitoring for Action (CARMA) Database (2009); www.carma.org.

71. H. Bovensmann et al., SCIAMACHY: Mission objectives and measurement modes. *J. Atmos. Sci.* **72**, 127–150 (2015).

72. H. Bovensmann, H. Bösch, D. Brunner, P. Ciais, D. Crisp, H. Dolman, G. Hayman, S. Houweling, L. Lichtenberg, "Report for mission selection: CarbonSat - An earth explorer to observe greenhouse gases" (European Space Agency, 2015); http://nora.nerc.ac.uk/514012/.

73. A. Eldering, S. Kaki, M. Bennett, "The Orbiting Carbon Observatory-3 (OCO-3) mission: An overview" (Fall Meeting abstract, American Geophysical Union, 2014).

74. NASA, "NASA announces first geostationary vegetation, atmospheric carbon mission" (NASA, 6 December 2016); www.nasa.gov/press-release/nasa-announces-first-geostationary-vegetation-atmospheric-carbon-mission).

75. I. N. Polonsky, D. M. O'Brien, J. B. Kumer, C. W. O'Dell, Performance of a geostationary mission, geoCARB, to measure CO_2, CH_4 and CO column-averaged concentrations. *Atmos. Meas. Tech.* **7**, 959–981 (2014). doi: 10.5194/amt-7-959-2014

SUPPLEMENTARY MATERIALS

www.sciencemag.org/content/358/6360/eaam5782/suppl/DC1
Fig. S1
References (*76–77*)

Science

Spaceborne detection of localized carbon dioxide sources

Florian M. Schwandner, Michael R. Gunson, Charles E. Miller, Simon A. Carn, Annmarie Eldering, Thomas Krings, Kristal R. Verhulst, David S. Schimel, Hai M. Nguyen, David Crisp, Christopher W. O'Dell, Gregory B. Osterman, Laura T. Iraci and James R. Podolske

ARTICLE TOOLS	http://science.sciencemag.org/content/358/6360/eaam5782
SUPPLEMENTARY MATERIALS	http://science.sciencemag.org/content/suppl/2017/10/12/358.6360.eaam5782.DC1
RELATED CONTENT	http://science.sciencemag.org/content/sci/358/6360/186.full http://science.sciencemag.org/content/sci/358/6360/eaam5745.full http://science.sciencemag.org/content/sci/358/6360/eaam5747.full http://science.sciencemag.org/content/sci/358/6360/eaam5776.full http://science.sciencemag.org/content/sci/358/6360/eaam5690.full
REFERENCES	This article cites 65 articles, 7 of which you can access for free http://science.sciencemag.org/content/358/6360/eaam5782#BIBL
PERMISSIONS	http://www.sciencemag.org/help/reprints-and-permissions